

## Revisiting Conversion Reaction Mechanisms in Lithium Batteries: Lithiation-Driven Topotactic Transformation in FeF

Khim Karki, Lijun Wu, Ying Ma, Mark J. Armstrong, Justin D. Holmes,  
Stephen H. Garofalini, Yimei Zhu, Eric A. Stach, and Feng Wang

*J. Am. Chem. Soc.*, **Just Accepted Manuscript** • DOI: 10.1021/jacs.8b07740 • Publication Date (Web): 20 Nov 2018

Downloaded from <http://pubs.acs.org> on November 20, 2018

### Just Accepted

“Just Accepted” manuscripts have been peer-reviewed and accepted for publication. They are posted online prior to technical editing, formatting for publication and author proofing. The American Chemical Society provides “Just Accepted” as a service to the research community to expedite the dissemination of scientific material as soon as possible after acceptance. “Just Accepted” manuscripts appear in full in PDF format accompanied by an HTML abstract. “Just Accepted” manuscripts have been fully peer reviewed, but should not be considered the official version of record. They are citable by the Digital Object Identifier (DOI®). “Just Accepted” is an optional service offered to authors. Therefore, the “Just Accepted” Web site may not include all articles that will be published in the journal. After a manuscript is technically edited and formatted, it will be removed from the “Just Accepted” Web site and published as an ASAP article. Note that technical editing may introduce minor changes to the manuscript text and/or graphics which could affect content, and all legal disclaimers and ethical guidelines that apply to the journal pertain. ACS cannot be held responsible for errors or consequences arising from the use of information contained in these “Just Accepted” manuscripts.

# Revisiting Conversion Reaction Mechanisms in Lithium Batteries: Lithiation-Driven Topotactic Transformation in FeF<sub>2</sub>

Khim Karki,<sup>\*,†,Ψ</sup> Lijun Wu,<sup>‡,Ψ</sup> Ying Ma,<sup>¥</sup> Mark J. Armstrong,<sup>£,δ</sup> Justin D. Holmes,<sup>£,δ</sup> Stephen H. Garofalini,<sup>φ</sup> Yimei Zhu,<sup>‡</sup> Eric A. Stach,<sup>§,ζ</sup> and Feng Wang<sup>\*,†</sup>

<sup>†</sup> Sustainable Energy Technologies Department, Brookhaven National Laboratory, Upton, New York, 11973, United States

<sup>‡</sup> Department of Condensed Matter Physics and Materials Science, Brookhaven National Laboratory, Upton, New York, 11973, United States

<sup>¥</sup> Materials Science & Engineering, University of Wisconsin-Eau Claire, Wisconsin, 54701, United States

<sup>£</sup> School of Chemistry and the Tyndall National Institute, University College Cork, Cork, T12 YN60, Ireland

<sup>δ</sup> AMBER@CRANN, Trinity College Dublin, Dublin 2, Ireland

<sup>φ</sup> Department of Materials Science and Engineering, Rutgers University, 607 Taylor Rd, Piscataway, NJ 08854, United States

<sup>§</sup> Center for Functional Nanomaterials, Brookhaven National Laboratory, Upton, New York, 11973, United States

<sup>ζ</sup> Department of Materials Science and Engineering, University of Pennsylvania, Philadelphia, PA 19104, United States

**KEYWORDS:** Lithium batteries, Conversion reaction mechanisms, Topotactic transformation, Iron fluorides (FeF<sub>2</sub>)

Intercalation-type electrodes have now been commonly employed in today's batteries due to their capability of storing and releasing lithium reversibly *via* topotactic transformation, conducive to small structural change, but they have limited interstitial sites to hold Li. In contrast, conversion electrodes feature high Li-storage capacity, but often undergo large structural change during (de)lithiation, resulting in cycling instability. One exception is iron fluoride (FeF<sub>2</sub>), a conversion-type cathode that exhibits both high capacity and high cycling stability. Herein, we report a lithiation-driven topotactic transformation in a single crystal of FeF<sub>2</sub>, unveiled by *in situ* visualization of the spatial and crystallographic correlation between the parent and converted phases. Specifically, conversion in FeF<sub>2</sub> resembles the intercalation process but involves transport of both Li<sup>+</sup> and Fe<sup>2+</sup> ions within the F-anion array, leading to formation of Fe preferentially along specific crystallographic orientations of FeF<sub>2</sub>. Throughout the process, the F-anion framework is retained, creating a checkerboard-like structure, within which the volume change is largely compensated, thereby enabling the high cyclability in FeF<sub>2</sub>. Findings from this study, with unique insights into conversion reaction mechanisms, may help to pave the way for designing conversion-type electrodes for the next-generation lithium batteries.

Conversion-based transition metal (TM) compounds, (TM)<sub>a</sub>X<sub>b</sub> (TM = Fe, Co, Ni, Cu; X = O, S, F, P, N), particularly oxides (*e.g.*, Fe<sub>3</sub>O<sub>4</sub>, CoO, NiO) and fluorides (FeF<sub>2</sub>, FeF<sub>3</sub>, CuFeF<sub>2</sub>) – have recently received enormous attention for use in lithium batteries because of their extremely high specific capacity (500–1000 mAh/g), 3–4 times greater than the intercalation compounds.<sup>1–6</sup> In contrast to intercalation-based electrodes, which function by shuttling lithium ions between the tunnels of the host through a topotactic transformation process, with causing significant structural changes,<sup>7</sup> electrochemical reactions in conversion-type electrodes are complex, involving migration/re-ordering of the TM ions, and eventually the extrusion of the metallic TMs (TM<sup>n+</sup>X<sub>y</sub> + nLi<sup>+</sup> + ne<sup>-</sup> = yLi<sub>n/y</sub>X + TM<sup>0</sup>; n ≥ 2), leading to significant<sup>6,8–10</sup> The converted products are spatially distributed and decoupled

from the parent host structure, leading to inhomogeneous phases, *e.g.* metallic TM and insulating LiX and, consequently, capacity loss of the electrode during subsequent reconversion and cycling processes.<sup>11, 12</sup> In addition, the large volume expansion that occurs during the conversion reaction leads to pulverization of the electrodes, and contributes further to the irreversibility of the reaction.<sup>6</sup> The low cycling reversibility of conversion electrodes has thus been a major impediment to their commercialization.<sup>11–16</sup>

Few conversion-based electrodes such as metal fluorides have shown exceptional cycling reversibility.<sup>8,9</sup> Notably, up to 1000 cycles has been demonstrated in FeF<sub>2</sub>,<sup>17</sup> which, along with the findings that voltage hysteresis is largely kinetic in nature<sup>9,12,14,18</sup>, indicates potential viability of the fluoride based battery systems for commercial use. High cycling reversibility

has also been reported in some conversion oxides<sup>10</sup> and displacement-type intermetallic compounds<sup>15</sup>. For instance, Zhang *et al.* observed retention of the cubic close-packed (*ccp*) O-anion framework of Fe<sub>3</sub>O<sub>4</sub> during the electrochemical cycling, thereby enabling multiple lithium intercalation and conversion reaction.<sup>10</sup> The electrochemical reaction in Fe<sub>3</sub>O<sub>4</sub> shows high similarity to that in displacement-type Li-Cu-Sb compounds, wherein remarkable cycling reversibility was observed and attributed to retaining the face-centered cubic (*fcc*) Sb structure through the conversion/reconversion processes.<sup>15</sup> Results from these studies indicate that the retention of the original structural framework is crucial to achieving high reversibility of electrodes. Despite these observations, the exact mechanisms that lead to the structural retention between the parent and product phases during the conversion reaction are not well understood.

Here, we present *real-time* observation of a conversion-driven topotactic phase transformation in a single crystal of FeF<sub>2</sub>, with preferential growth of Fe phase along specific crystallographic orientations of the parent FeF<sub>2</sub>, using *in situ* transmission electron microscopy (TEM) techniques.<sup>9,19,20</sup> Topotactic-mode of phase transformation is usually observed at high temperatures and during the process the product phase evolves from the reactant parent substrate by maintaining structural symmetry between the two.<sup>21</sup> Some other cases where topotactic reaction mechanisms have been reported are oxidation-reduction of metal oxides,<sup>22–24</sup> dehydration reactions,<sup>21,24</sup> polymeric phase transformations,<sup>24,25</sup> nanostructured synthesis,<sup>26,27</sup> and growth of thin films (EuO from the reduction of Eu<sub>2</sub>O<sub>3</sub>).<sup>28</sup> Electrochemical intercalation *via* shuttling lithium ions between the tunnels of the host is another special case of topotactic transformation.<sup>7</sup> However, such a conversion-driven topotactic growth of Fe from FeF<sub>2</sub> is totally unexpected because the two have a completely different structure, and the reaction occurs at room temperature (RT). Although extensive *in situ* studies have been performed on FeF<sub>2</sub> (or its derivatives), such a conversion-driven topotactic process has never been reported.<sup>8,9,17,29–32</sup> On one hand, conversion-type reaction is complex, involving multiphase transformations and local transport of cations and lithium ions within nano-sized domains. On the other hand, powder or polycrystalline materials have mostly been employed in studies of these processes, and the random orientation of constituent crystallites obscures the topotactic relationships as they develop.<sup>8,9</sup> The use of single-crystalline FeF<sub>2</sub> particles in this study allows tracking of the crystallographic evolution of the involved phases, *i.e.* the progression of the lithium conversion reaction along specific crystallographic orientations.

For this study, plate-like FeF<sub>2</sub> single-crystalline particles were synthesized by a supercritical fluid method (See Supporting Information, Figure S1).<sup>33</sup> Figure 1a shows the bright-field TEM image of a typical FeF<sub>2</sub> particle, which is oriented along the [001] crystallographic direction, as verified by electron diffraction (Figure 1b). The FeF<sub>2</sub> single-crystal appears to have a primary growth axis along the [110] direction, with two small facets along (0 $\bar{2}$ 0) and ( $\bar{2}$ 00), and a longer facet running along ( $\bar{1}$ 10). Because FeF<sub>2</sub> is an electrical insulator,<sup>4</sup> to improve the electrical conductivity, the surface of FeF<sub>2</sub> particle was coated with a thin layer of carbon (See

Supporting Information; Section I). The progression of the lithium reaction in FeF<sub>2</sub> is tracked by the *in situ* TEM method with individual particles brought in point contact with the lithium source (See Supporting Information, Section II, Figure S2, and Movie M1). TEM images were recorded at a frequency of 5 frames per second from a local area that is approximately 33 nm wide, and 33 nm long (as marked by red frame in Figure 1a). Some of the sequential images extracted from Movie M1 are shown in Fig. 1c. Upon applying the bias, the conversion occurs first from the surface region due to fast Li diffusion along the surface. Those converted Fe nanoparticles, being discerned by dark contrast under the bright field (BF) condition, form a percolating network, and so serve as the conducting pathway for electronic transport.<sup>34, 35</sup> As the reaction proceeds further into the bulk, a well-aligned and repeating fringe-like pattern grows as an overlayer on the <110> FeF<sub>2</sub>. The Fe domains are formed periodically, as indicated by arrows in the images taken following 2s, 4s, 5s, 6s, 10s, 17s and 30s of lithiation, respectively. The reaction front propagates gradually from surface to the bulk, layer-by-layer (Figure 1c; as illustrated by blue arrows).<sup>34,35</sup>

To identify the local structural change, high-resolution TEM (HRTEM) images were taken in the pristine state from selected small area ( $t = 0$  s; marked by a blue frame in Figure 1a), and after full lithiation ( $t = 30$  s; provided in Figure d and f respectively). The pristine FeF<sub>2</sub> is highly crystalline, as shown by the fast Fourier transform (FFT; inset) of the HRTEM image, and its lattice is highly-ordered as seen from the inverse FFT image (Figure 1e; from the local area labelled by the dotted box in Figure 1d). Upon lithium conversion, FeF<sub>2</sub> turns into a network of nanoscale Fe domains, similar to what was observed in the previous studies on small FeF<sub>2</sub> nanoparticles<sup>8,9,36</sup> but they appear to arrange in a fringe-like pattern, as shown in Figure 1f. At this stage, the initial periodic arrangement of FeF<sub>2</sub> is disrupted and forms a highly strained interconnected network of Fe nano-domains surrounded by random dislocations (denoted as “T”), as clearly shown in the inverse FFT image in Figure 1g (extracted from the dotted frame area in Figure 1f). The characteristic fringe-like pattern of newly formed Fe suggests Fe grows with preferential orientation with respect to the underlayer FeF<sub>2</sub> – in this case along [110] direction of the parent FeF<sub>2</sub> (as to be discussed below).

To elucidate the structural correlation between Fe and the parent FeF<sub>2</sub>, time-resolved *in situ* electron diffraction measurements were performed (See Supporting Information, Section II). Figure 2a presents a time-sequence of electron diffraction patterns, captured from a local area on the same single-crystalline FeF<sub>2</sub> particle but further away from the area for *in situ* HRTEM measurements (see also Supporting Information, Movie M2). The corresponding azimuthal projection of the diffraction patterns ( $x$ -axis=angle,  $y$ -axis=radius) was extracted (Figure 2b) to determine all of the peak parameters *via* a precise profile analysis (intensity vs. diffraction) of the selected area diffraction pattern using the PASAD-tools software.<sup>37</sup>

Prior to lithiation ( $t = 0$  s), characteristic diffraction spots for single-crystalline FeF<sub>2</sub> particle are observed along the [001] zone axis. As the lithiation progresses, four new, broad, arc-shaped diffraction spots appear, faint initially and becoming

stronger with time (Supporting Movie M2). By  $t = 8$  min, the arc-shaped spots can be clearly seen at positions adjacent to the spots of  $\{200\}\text{FeF}_2$  (as labeled by green arrows in Figure 2a) and better resolved in the corresponding projected patterns in Figure 2b. The arc-shaped diffraction spots represent a mosaic of tiny Fe crystallites,<sup>24</sup> with a four-fold symmetry (indexed to the  $\{110\}\text{Fe}$  family of planes), thus indicating a topotactic relationship between the converted Fe and the parent  $\text{FeF}_2$ .<sup>21</sup> Although the coherent nature of Fe crystallites was observed previously,<sup>8,9</sup> topotactic growth of Fe from the parent  $\text{FeF}_2$  is surprising and, indeed unexpected, considering that the two have a completely different structure (bcc vs. tetragonal). Furthermore, the topotactic conversion reaction occurs at RT -- starkly different from the traditional epitaxial<sup>38</sup> or topotactic<sup>21,24</sup> growth at high temperatures. It should be noted that the use of a single crystal is crucial to deconvoluting this information in this *in situ* study, thereby allowing us to observe the evolving crystallographic relationship in detail. The majority of the Fe that is formed (as labeled with green arrows; Case - I from hereafter), tends to have a strong orientation relationship with the parent  $\text{FeF}_2$ , such that  $[001]\text{Fe-I} \parallel [001]\text{FeF}_2$ ,  $[110]\text{Fe-I} \parallel [010]\text{FeF}_2$  and  $[\bar{1}\bar{1}0]\text{Fe-I} \parallel [100]\text{FeF}_2$  (Fe-I and  $\text{FeF}_2$  represent Case-I Fe domains and  $\text{FeF}_2$ , respectively). Interestingly, there are also additional set of arcs associated with Fe, as indicated by red arrows (Case - II from hereafter), demonstrating the presence of a second form of topotactic Fe growth, aligned with  $\text{FeF}_2$  by a new relationship:  $[101]\text{Fe-II} \parallel [001]\text{FeF}_2$ ,  $[010]\text{Fe-II} \parallel [110]\text{FeF}_2$  and  $[\bar{1}01]\text{Fe-II} \parallel [1\bar{1}0]\text{FeF}_2$ . Note,  $[020]\text{Fe-II}$  is along the Li diffusion direction. While faint and somewhat diffuse at this stage of the process, they do not have a four-fold symmetry (as in Case-I). Such a topotactic evolution of Fe over the parent  $\text{FeF}_2$  (Cases I & II) was commonly observed in this experiment; see also another set of diffraction data recorded along  $[001]$  oriented  $\text{FeF}_2$  in Supporting Information, Figure S3.

During further lithiation (from  $t = 17'$  to  $19'$ ), Fe grains grew with the consumption of the parent  $\text{FeF}_2$ , and correspondingly, those arc-shaped diffraction spots became stronger, and the spots associated with  $\text{FeF}_2$  became weaker. Figure 2c shows the progression of the spot intensity for  $(1\bar{1}0)\text{Fe}$  and  $(\bar{1}01)\text{Fe}$  as a function of lithiation time, in comparison to that of the parent  $(200)\text{FeF}_2$  spot. As demonstrated by the intensity profiles, the  $(1\bar{1}0)\text{Fe}$  spot, which represents the Case I (green arrows) orientation relationship, is dominant over the  $(\bar{1}01)\text{Fe}$ , which represents Case II (red arrows). In both Cases I and II, there are large spikes in the intensities of Fe reflections at the initial state of lithiation. However, after 17 min, the reflection intensities for both cases saturate and fade in a gradual manner. The growth of Fe grain with lithiation introduces lattice distortion, yielding dislocations (Figure 1g) and coarsening of the Fe domains, which is likely responsible for deceleration of the kinetics of conversion reaction in the bulk.<sup>11,39</sup>

The overall phase evolution during lithiation was also examined by obtaining the integrated intensity profiles from the entire diffraction patterns (full rings); see Figure 2d, e. Clearly, the reflections associated with the parent  $\text{FeF}_2$  are initially intense, and as the lithiation progresses, they become weaker; while the broad Fe peaks become stronger. We did not observe an obvious shift in the peak position of the

$(200)\text{FeF}_2$ , indicating no lattice distortion or expansion within the resolution limits of the diffraction technique,<sup>9</sup> although there have been speculations regarding the possibility of lithium intercalation during the initial lithiation.<sup>32,34,35,39</sup> While the  $(110)\text{Fe}$  peaks shift towards higher angles in the early stage, likely due to the formation of small Fe crystallites with slight lattice expansion, as observed previously.<sup>9</sup>

To corroborate the *in situ* TEM observations, we performed *ex situ* TEM analysis on electrochemically discharged  $\text{FeF}_2$  via a quasi *in situ* TEM coin-cell technique<sup>40</sup> (See Supporting Information, Section III and Figure S4). A typical BF TEM image from a partially-discharged  $\text{FeF}_2$  particle, and the corresponding diffraction pattern taken from the local area (as marked by dotted circle) are given in Figures 3a, b. Clearly the diffraction pattern shows the similar features as that in the *in situ* measurements (Figure 2), further validating the *in situ* observation of the topotactic growth of Fe from the parent  $\text{FeF}_2$ . Figure 3c presents the integrated intensities from the  $(1\bar{1}0)\text{Fe}$  (Case-I) and  $(\bar{1}01)\text{Fe}$  (Case-II) reflections. The higher intensity of the  $(1\bar{1}0)\text{Fe}$  (Case-I) reflection indicates that this orientation relationship is more frequent in the sample. Figure 3d is a magnified image extracted from the yellow framed area of Figure 3a. There is a similar fringe-like pattern as found in Figures (1c, 1d). This pattern was interpreted to be a result of preferential formation of Fe along specific orientation of  $\text{FeF}_2$ . The FFT of the given area, which is shown in the inset, is similar to the diffraction patterns extracted from the large area (Figure 3b). However, the fringe-like pattern observed in the *ex situ* studies is similar to that that observed at 30s during the *in situ* experiment (Figure 1g), which should be due to the relaxation effect, after removal of the electric bias in the coin cell.

Interestingly, one would expect that Fe is least mobile given its large atomic mass and the strong  $\text{Fe}^{2+} - \text{F}^-$  ionic bonding. However, it has been shown that  $\text{Fe}^{2+}$  ions are quickly reduced to neutral  $\text{Fe}^0$  upon lithiation,<sup>34</sup> which essentially breaks the Fe-F bonds and results in  $\text{Fe}^0$  atoms that are bonded neither to  $\text{Li}^+$  nor  $\text{F}^-$ . Thus,  $\text{Fe}^0$  atoms diffuse freely out of the mixture and form the metallic phase. To confirm this, reactive molecular dynamics (MD) simulations<sup>34</sup> were performed, with the results showing that the diffusion coefficient of  $\text{Fe}^0$  is dramatically increased as compared to that of  $\text{Fe}^{2+}$ , and  $\text{Fe}^0$  is, indeed, the most mobile species (Supporting Information, Section IV and Table S1). This is important, as this observation suggests that the growth of the Fe from  $\text{FeF}_2$  is driven by electrochemical lithiation at RT, which leads to the reduction of  $\text{Fe}^{2+}$ . Considering the difference in diffusivity, the lithium conversion reaction along the  $[001]$   $\text{FeF}_2$  direction must involve the reduction and then diffusion of Fe as well as the local displacement and ordering of  $\text{Li}^+$  within the close-packed F-anion framework since both  $\text{Li}^+$  and  $\text{F}^-$  have a much smaller diffusion coefficient. So, based on the *in situ* observations, we attempt to develop a structural model to explain the observed conversion-driven topotactic phase transformation in  $\text{FeF}_2$ .

Figure 4a presents a 3D view of the  $\text{FeF}_2$  structure, with alternative layers of  $\text{FeF}_2$  along  $[001]$  direction in the unit cell. Two large channels exist in the  $[001]$  and  $[110]$  directions, and it has been shown that  $[001]$  is energetically more favorable for

lithium ion diffusion.<sup>34,39</sup> Lithium insertion along the [001] direction (top or bottom surface of FeF<sub>2</sub> particle) would push the Fe out either in the [010] or [100] direction, while the inserted Li ions would likely occupy the center of the trapezoid constructed by the F atoms, as shown in Figure 4b. Note that because LiF will expand along the *c* direction, there is no room for Fe to move toward the *c* direction. Because the bonding length of LiF is about 0.2 nm (based on its bulk structure), it would shrink along both *a* and *b* direction, while expanding along the *c* direction to form Li-F bonding, as shown in Figure 4c. Once Fe is out of FeF<sub>2</sub> lattice, it would alternately shift about 0.2 nm along the *a* direction to form Fe-Fe bonding due to the strong force along the *b* direction, as shown in Figure 4b. The (001) Fe layer would then contract to form a Fe lattice, as shown in Figure 4c. The resulting local cationic displacement and reordering will result in the following relationship between the Fe and FeF<sub>2</sub> lattices: [001]Fe-I || [001]FeF<sub>2</sub>, [110]Fe-I || [010]FeF<sub>2</sub>, [110]Fe-I || [100]FeF<sub>2</sub>, as experimentally observed (Case - I) The expansion/contraction of Fe/LiF is different along two different directions during the phase transformation of FeF<sub>2</sub> + 2Li<sup>+</sup> + 2e<sup>-</sup> → Fe + 2LiF. The phase transformation results in expansion along the *b* direction, contraction along the *a* direction, and expansion along the *c* direction for LiF, but contraction for Fe. Note that due to the four-fold symmetry of FeF<sub>2</sub>, Fe can be equivalently pushed out along the [100] direction. In this case, we get another orientation relationship: [001]Fe-I' || [001]FeF<sub>2</sub>, [110]Fe-I' || [100]FeF<sub>2</sub> and [110]Fe-I' || [010]FeF<sub>2</sub> (Fe-I' represents the equivalent Case-I Fe domain). The diffraction spots of the Fe-I' domain would overlap with those of the Fe-I domain. The expansion/contraction of the Fe-I' domain is the same as that of the Fe-I domain except it expands along the *a* direction but contracts along the *b* direction. Therefore, the converted LiF and Fe likely form a checkerboard-like pattern in all three directions, as illustrated in Figure 4d, in which the expansion/contractions are compensated to fit the 3D space. The domain size of Fe/LiF would thus be very small and difficult to grow. Interestingly, the Fe lattice fringes that are observed along the [110] direction in the thin area during the lithiation conversion process in Figures 1c and 1f are consistent with this checkerboard-like arrangement of Fe/LiF domains. Because of the four-fold symmetry of FeF<sub>2</sub>, the Fe fringes can align parallel to [110] direction. The two orientated Fe fringes may overlap along the beam direction. This would form a two-dimensional pattern, but image evidence for this would be less pronounced when the sample is thick.

Alternatively, Li insertion along the [110] FeF<sub>2</sub> direction (from the side surfaces of the FeF<sub>2</sub> particle in Figure 1a) would push the Fe out along the [110] FeF<sub>2</sub> direction (See Supporting Information, Figure S5). In this case, LiF would shrink along both [110] and [110] directions, while expanding along the *c* direction to form Li-F bonding, as shown in Figure S5c. Similarly, the spacing of the Fe layers would expand vertically to form an Fe lattice. In this case, the relationship between the Fe and FeF<sub>2</sub> lattice is: [101]Fe-II || [001]FeF<sub>2</sub>, [010]Fe-II || [110]FeF<sub>2</sub>, and [101]Fe-II || [110]FeF<sub>2</sub>. Because the insertion of Li along the [110] direction is more difficult than that along the [001] direction,<sup>34,39</sup> a driving force is needed to make this conversion happen. Thus, it is logical that we only see the Fe-

II domains with an orientation of [010]Fe-II along the [110]FeF<sub>2</sub> direction, which is the direction of Li diffusion in the FeF<sub>2</sub> particle. The likelihood of forming this kind of domain would also be low, consistent with the faint diffraction spots (red arrows) present in Figure 2. As evident from Figure S6, the distribution of Fe that has the Case I orientation is dominant when compared to Case II, agreeing well with both the experimental data and the structural analysis presented above. These results are also consistent with earlier computational modeling where the lithiation along the [110] direction was observed to be very limited as compared to that along the [001] direction.<sup>34</sup>

The lithiation process in the plate-like single crystalline particle proceeds *via* layer-by-layer, from surface to the bulk (as in Figure 1), similar to the observation on small FeF<sub>2</sub> nanoparticles (10-20nm) despite the different shapes<sup>8,9</sup>. The high similarity is due to the fact that FeF<sub>2</sub> is an insulator, the reaction front propagates, "layer-by-layer", into the bulk, during which the Fe percolating network is gradually built up to provide electronic transport pathway. The plate-like shape also allows easy access to lithium, similar to that in the small nanoparticles. In addition, the formation of the percolating Fe network after lithiation resembles the previous *ex situ*<sup>8</sup> and *in situ*<sup>9</sup> observations from small nanoparticles. But, by using a plate-like particle, we were able to reveal more details of the lithiation process forming checkerboard-like structure wherein volume change is largely compensated, thus enabling structural integrity and cycling stability in such conversion-type electrodes.

And importantly, the use of single-crystal samples allowed us to reveal the crystallographic correlation between the involved intermediates, namely topotactic transformation process, which was not observed in the previous studies. The observation in this study also explains the coherent nature of the converted Fe crystallites reported in the previous studies.<sup>8,9</sup> On the other hand, such an unexpected topotactic conversion process resembles the conventional intercalation process, suggesting that conversion in FeF<sub>2</sub> proceeds *via* cooperative ionic transport of Li<sup>+</sup> and Fe<sup>2+</sup> within the close-packed F-anion array, with the framework retained throughout the process (so resembling the intercalation process). In a traditional view, the electrochemical reaction in electrodes either occurs *via* intercalation process, namely insertion of Li<sup>+</sup> ions into interstitial sites without breaking the crystal lattice of the host, or *via* conversion that involves local migration/re-ordering of transition metal (TM) ions, and eventually, the extrusion of metallic TMs. Results from this study imply that these two types of reaction may be viewed the same, both through topotactic transformation process involving ionic transport and ordering of cations (Li<sup>+</sup> and TM ions) in a close-packed anion framework. These findings may explain the origin of high cyclability in FeF<sub>2</sub> *via* topotactic mechanism since the structural relationship between the parent and converted species are preserved and presumably provides reaction pathway for further reconversion during cycling.

Whereas the neutral Fe atoms are the most mobile, charged ions, including Li<sup>+</sup> and F<sup>-</sup>, are expected to have increased diffusion coefficients due to the presence of the external field. Formation of intermediate phases during

reconversion is also possible, which is supported by both experimental<sup>12,14</sup> and theoretical<sup>41</sup> evidences. These differences could give rise to a distinct reaction mechanism for reconversion. It would be desirable to track the reconversion process *via in situ* TEM method, but difficult with the current setup. A few studies using single nanowire based batteries and using LiPON-based electrolyte in the TEM have shown promising in achieving full charge/discharge cycle.<sup>42,43</sup> Nonetheless, it is challenging to accommodate and manipulate single-crystalline particles as shown in the current study. In order to observe the re-conversion process, a completely different *in situ* TEM platform, incorporated with robust solid electrolyte and single-crystalline particles with desired orientation, needs to be developed.

In summary, through *in situ* observation of lithiation process in single-crystalline FeF<sub>2</sub>, we revealed conversion-driven topotactic transformation. During the process, the converted Fe phase is not randomly oriented as traditionally believed, but preferentially aligned along specific crystallographic orientations of the parent FeF<sub>2</sub>. Structural modeling suggests the formation of a checkerboard-like arrangement of Fe/LiF domains upon topotactic displacement of Fe from the parent FeF<sub>2</sub>. Consequently, a percolating 3D network of Fe and LiF is formed, which may explain the previous observation of bi-continuous network, a pathway for local electron transport. These observations present unique insights into the conversion reaction mechanisms, and so may help to pave the way for designing conversion-type electrodes for high energy density lithium batteries.

## ASSOCIATED CONTENT

### Supporting Information

Materials preparation procedures, X-ray diffraction data and scanning electron microscopy images of the synthesized FeF<sub>2</sub> particles, *in situ* TEM experimental methods, electrochemical discharge/*ex situ* TEM diffraction, molecular dynamic simulations are included in the supporting information. This material is available free of charge via the Internet at <http://pubs.acs.org>.

## AUTHOR INFORMATION

### Corresponding Author

kkarki@bnl.gov  
fwang@bnl.gov

### Author Contributions

<sup>‡</sup> These authors contributed equally.

### Notes

The authors declare no competing financial interests.

## ACKNOWLEDGMENT

This work is financially supported by Northeastern Center for Chemical Energy Storage, an Energy Frontier Research Center funded by the U.S. DOE, BES under award number DE-

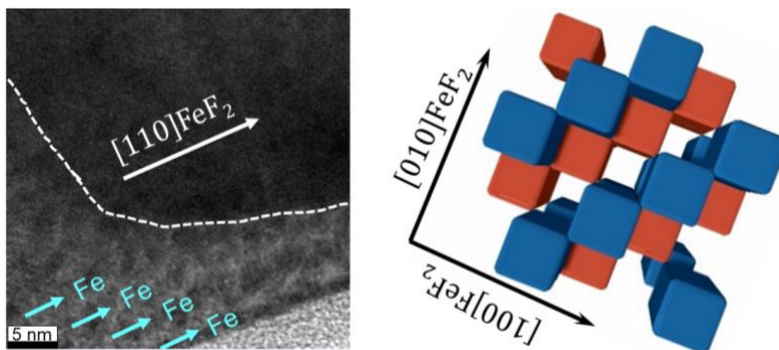
SC0001294. This research used resources of the Center for Functional Nanomaterials, which is a U.S. DOE Office of Science Facility, at Brookhaven National Laboratory under Contract No. DE-SC0012704. Lijun Wu and Yimei Zhu were supported by the U.S. Department of Energy, Office of Basic Energy Science, Division of Materials Science and Engineering, under Contract No. DE-SC0012704. MJA and JDH acknowledge financial support from Science Foundation Ireland (Project: 07/SRC/I1172). We thank Tiffany Bowman for the graphic design of the TOC.

## REFERENCES

- (1) Li, C.; Chen, K.; Zhou, X.; Maier, J. *npj Comput. Mater.* **2018**, *4* (1), 22.
- (2) Yu, S.-H.; Feng, X.; Zhang, N.; Seok, J.; Abruña, H. D. *Acc. Chem. Res.* **2018**, *51* (2), 273.
- (3) Wang, F.; Kim, S.-W.; Seo, D.-H.; Kang, K.; Wang, L.; Su, D.; Vajo, J. J.; Wang, J.; Graetz, J. *Nat Commun* **2015**, *6*.
- (4) Badway, F.; Cosandey, F.; Pereira, N.; Amatucci, G. G. *J. Electrochem. Soc.* **2003**, *150* (10), A1318.
- (5) Poizot, P.; Laruelle, S.; Grugeon, S.; Dupont, L.; Tarascon, J.-M. *Nature* **2000**, *407* (6803), 496.
- (6) Cabana, J.; Monconduit, L.; Larcher, D.; Palacin, M. R. *Adv. Mater.* **2010**, *22* (35), E170.
- (7) Whittingham, M. S. *Chem. Rev.* **2014**, *114* (23), 11414.
- (8) Wang, F.; Robert, R.; Chernova, N. A.; Pereira, N.; Omenya, F.; Badway, F.; Hua, X.; Ruotolo, M.; Zhang, R.; Wu, L.; Volkov, V.; Su, D.; Key, B.; Whittingham, M. S.; Grey, C. P.; Amatucci, G. G.; Zhu, Y.; Graetz, J. *J. Am. Chem. Soc.* **2011**, *133* (46), 18828.
- (9) Wang, F.; Yu, H.-C.; Chen, M.-H.; Wu, L.; Pereira, N.; Thornton, K.; Van der Ven, A.; Zhu, Y.; Amatucci, G. G.; Graetz, J. *Nat Commun* **2012**, *3*, 1201.
- (10) Zhang, W.; Bock, D. C.; Pelliccione, C. J.; Li, Y.; Wu, L.; Zhu, Y.; Marschilok, A. C.; Takeuchi, E. S.; Takeuchi, K. J.; Wang, F. *Adv. Energy Mater.* **2016**, *6* (10), 1502471.
- (11) Yu, H.-C.; Wang, F.; Amatucci, G. G.; Thornton, K. *J. Phase Equilibria Diffus.* **2016**, *37* (1), 86.
- (12) Li, L.; Jacobs, R.; Gao, P.; Gan, L.; Wang, F.; Morgan, D.; Jin, S. *J. Am. Chem. Soc.* **2016**, *138* (8), 2838.
- (13) Doe, R. E.; Persson, K. A.; Meng, Y. S.; Ceder, G. *Chem. Mater.* **2008**, *20* (16), 5274.
- (14) Ko, J. K.; Wiaderek, K. M.; Pereira, N.; Kinnibrugh, T. L.; Kim, J. R.; Chupas, P. J.; Chapman, K. W.; Amatucci, G. G. *ACS Appl. Mater. Interfaces* **2014**, *6* (14), 10858.
- (15) Chang, D.; Chen, M.-H.; Van der Ven, A. *Chem. Mater.* **2015**, *27* (22), 7593.
- (16) Kim, S.; Liu, J.; Sun, K.; Wang, J.; Dillon, S. J.; Braun, P. V. *Adv. Funct. Mater.* **2017**, 1702783.
- (17) Gu, W.; Borodin, O.; Zdyrko, B.; Lin, H.-T.; Kim, H.; Nitta, N.; Huang, J.; Magasinski, A.; Milicev, Z.; Berdichevsky, G.; Yushin, G. *Adv. Funct. Mater.* **2016**, *26* (10), 1507.
- (18) Liu, P.; Vajo, J. J.; Wang, J. S.; Li, W.; Liu, J. *J. Phys. Chem. C* **2012**, *116* (10), 6467.
- (19) Huang, J. Y.; Zhong, L.; Wang, C. M.; Sullivan, J. P.; Xu, W.; Zhang, L. Q.; Mao, S. X.; Hudak, N. S.; Liu, X. H.; Subramanian, A.; Fan, H.; Qi, L.; Kushima, A.; Li, J. *Science* (80-. ). **2010**, *330* (6010), 1515.
- (20) Karki, K.; Epstein, E.; Cho, J.-H.; Jia, Z.; Li, T.; Picraux, S. T.; Wang, C.; Cumings, J. *Nano Lett.* **2012**, *12* (3), 1392.
- (21) Shannon, R. D.; Rossi, R. C. *Nature* **1964**, *202* (4936), 1000.
- (22) Revcolevschi, A.; Dhalle, G. *Nature* **1985**, *316*, 335.
- (23) Cahn, R. W. *Nature* **1985**, *316* (6026), 297.
- (24) Figlarz, M.; Gérard, B.; Delahaye-Vidal, A.; Dumont, B.; Harb, F.; Coucou, A.; Fievet, F. *Solid State Ionics* **1990**, *43*,

143.  
1 (25) Söderquist, R.; Dickens, B. J. *Phys. Chem. Solids* **1967**, *28* (5),  
2 823.  
3 (26) Meng, F.; Morin, S. A.; Jin, S. *J. Am. Chem. Soc.* **2011**, *133* (22),  
4 8408.  
5 (27) Moon, G. D.; Ko, S.; Min, Y.; Zeng, J.; Xia, Y.; Jeong, U. *Nano*  
6 *Today* **2011**, *6* (2), 186.  
7 (28) Mairoser, T.; Mundy, J. A.; Melville, A.; Hodash, D.; Cueva,  
8 P.; Held, R.; Glavic, A.; Schubert, J.; Muller, D. A.; Schlom, D.  
9 G.; Schmehl, A. *Nat. Commun.* **2015**, *6*, 7716.  
10 (29) He, K.; Zhang, S.; Li, J.; Yu, X.; Meng, Q.; Zhu, Y. Y.; Hu, E.;  
11 Sun, K.; Yun, H.; Yang, X.-Q.; Zhu, Y. Y.; Gan, H.; Mo, Y.;  
12 Stach, E. A.; Murray, C. B.; Su, D. *Nat Commun* **2016**, *7*, 11441.  
13 (30) Li, L.; Chen-Wiegart, Y. K.; Wang, J.; Gao, P.; Ding, Q.; Yu,  
14 Y.-S.; Wang, F.; Cabana, J.; Wang, J.; Jin, S. *Nat Commun*  
15 **2015**, *6*.  
16 (31) Wiaderek, K. M.; Borkiewicz, O. J.; Castillo-Martínez, E.;  
17 Robert, R.; Pereira, N.; Amatucci, G. G.; Grey, C. P.; Chupas,  
18 P. J.; Chapman, K. W. *J. Am. Chem. Soc.* **2013**, *135* (10), 4070.  
19 (32) Yamakawa, N.; Jiang, M.; Key, B.; Grey, C. P. *J. Am. Chem.*  
20 *Soc.* **2009**, *131* (30), 10525.  
21 (33) Armstrong, M. J.; Panneerselvam, A.; O'Regan, C.; Morris, M.  
22 A.; Holmes, J. D. *J. Mater. Chem. A* **2013**, *1* (36), 10667.  
23 (34) Ma, Y.; Garofalini, S. H. *J. Am. Chem. Soc.* **2012**, *134* (19), 8205.  
24  
25  
26  
27  
28  
29  
30  
31  
32  
33  
34  
35  
36  
37  
38  
39  
40  
41  
42  
43  
44  
45  
46  
47  
48  
49  
50  
51  
52  
53  
54  
55  
56  
57  
58  
59  
60
- (35) Thorpe, R.; Rangan, S.; Whitcomb, R.; Basaran, A. C.;  
Saerbeck, T.; Schuller, I. K.; Bartynski, R. A. *Phys. Chem.*  
*Chem. Phys.* **2015**, *17* (23), 15218.  
(36) Li, L.; Meng, F.; Jin, S. *Nano Lett.* **2012**, *12* (11), 6030.  
(37) Gammer, C.; Mangler, C.; Rentenberger, C.; Karnthaler, H. P.  
*Scr. Mater.* **2010**, *63* (3), 312.  
(38) Tang, L.; Feng, Y. C.; Lee, L.-L.; Laughlin, D. E. *J. Appl.*  
*Crystallogr.* **1996**, *29* (4), 419.  
(39) Ma, Y.; Garofalini, S. H. *Phys. Chem. Chem. Phys.* **2014**, *16*  
(23), 11690.  
(40) Lin, F.; Nordlund, D.; Weng, T.-C.; Zhu, Y.; Ban, C.; Richards,  
R. M.; Xin, H. L. *Nat Commun* **2014**, *5*.  
(41) Ma, Y.; Garofalini, S. H. *J. Phys. Chem. C* **2017**, *121* (28), 15002.  
(42) Ruzmetov, D.; Oleshko, V. P.; Haney, P. M.; Lezec, H. J.;  
Karki, K.; Baloch, K. H.; Agrawal, A. K.; Davydov, A. V.;  
Krylyuk, S.; Liu, Y.; Huang, J.; Tanase, M.; Cumings, J.; Talin,  
A. A. *Nano Lett.* **2012**, *12* (1), 505.  
(43) Santhanagopalan, D.; Qian, D.; McGilvray, T.; Wang, Z.;  
Wang, F.; Camino, F.; Graetz, J.; Dudney, N.; Meng, Y. S. *J.*  
*Phys. Chem. Lett.* **2014**, *5* (2), 298.

## TOC Graphic



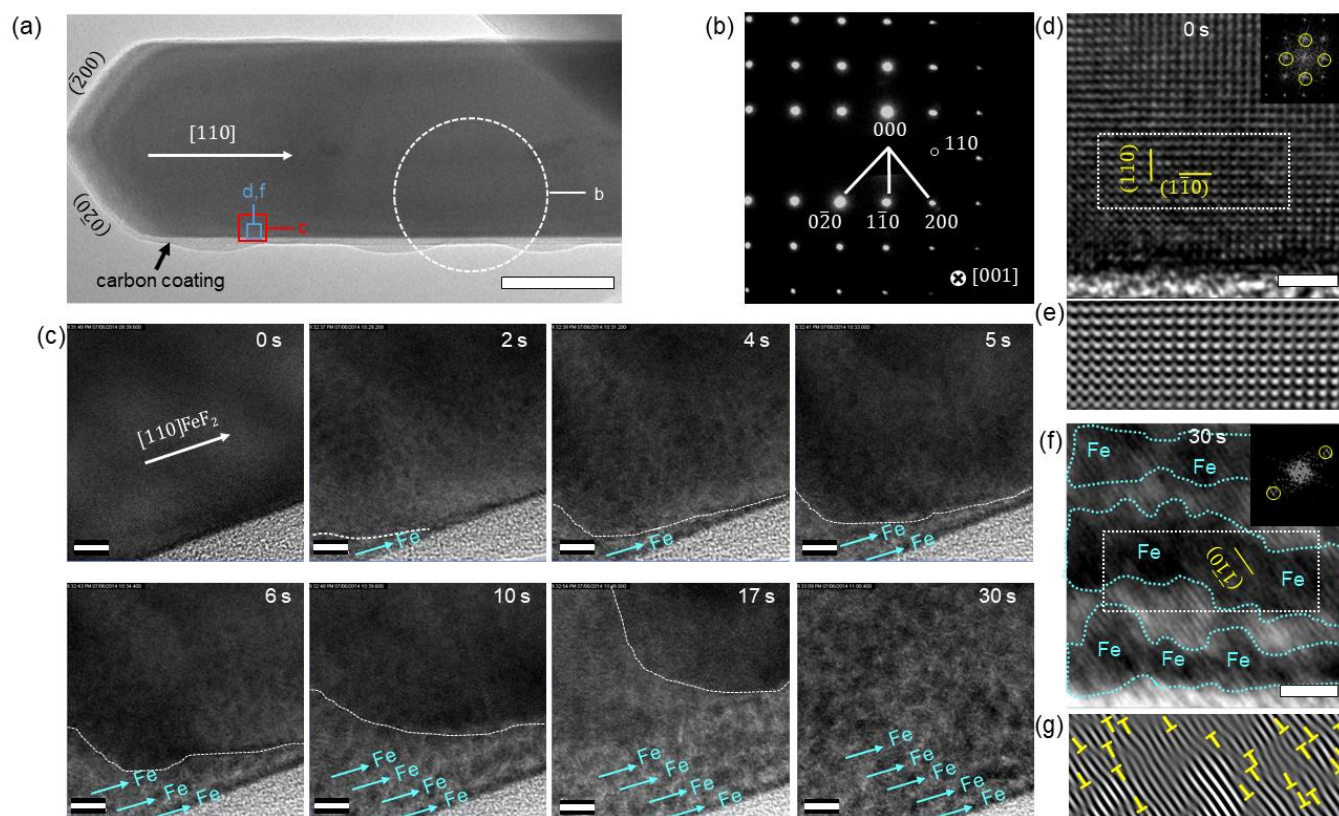


**Figure 1. Lithium conversion and phase propagation within a single crystal of  $\text{FeF}_2$ .** (a, b) Bright-field TEM image of a typical single-crystalline  $\text{FeF}_2$  particle and the corresponding electron diffraction pattern taken from a local region (as labeled by a circle in (a)). Scale bar: 100 nm. (c) Time-lapse TEM images from a local area (as labeled in a) during lithiation (See Supporting Movie M1). Scale bar: 5 nm. (d, e) HRTEM images of pristine  $\text{FeF}_2$  ( $t = 0$  s) from the blue framed region in (a), and an inverse FFT image from the selected white framed area. Scale bar: 2 nm. (f) HRTEM image of lithiated  $\text{FeF}_2$  (at  $t = 30$  s), from the same blue framed area in (a). Scale bar: 2 nm. (g) Inverse FFT image from the selected white framed area showing dislocations (denoted as “T”).

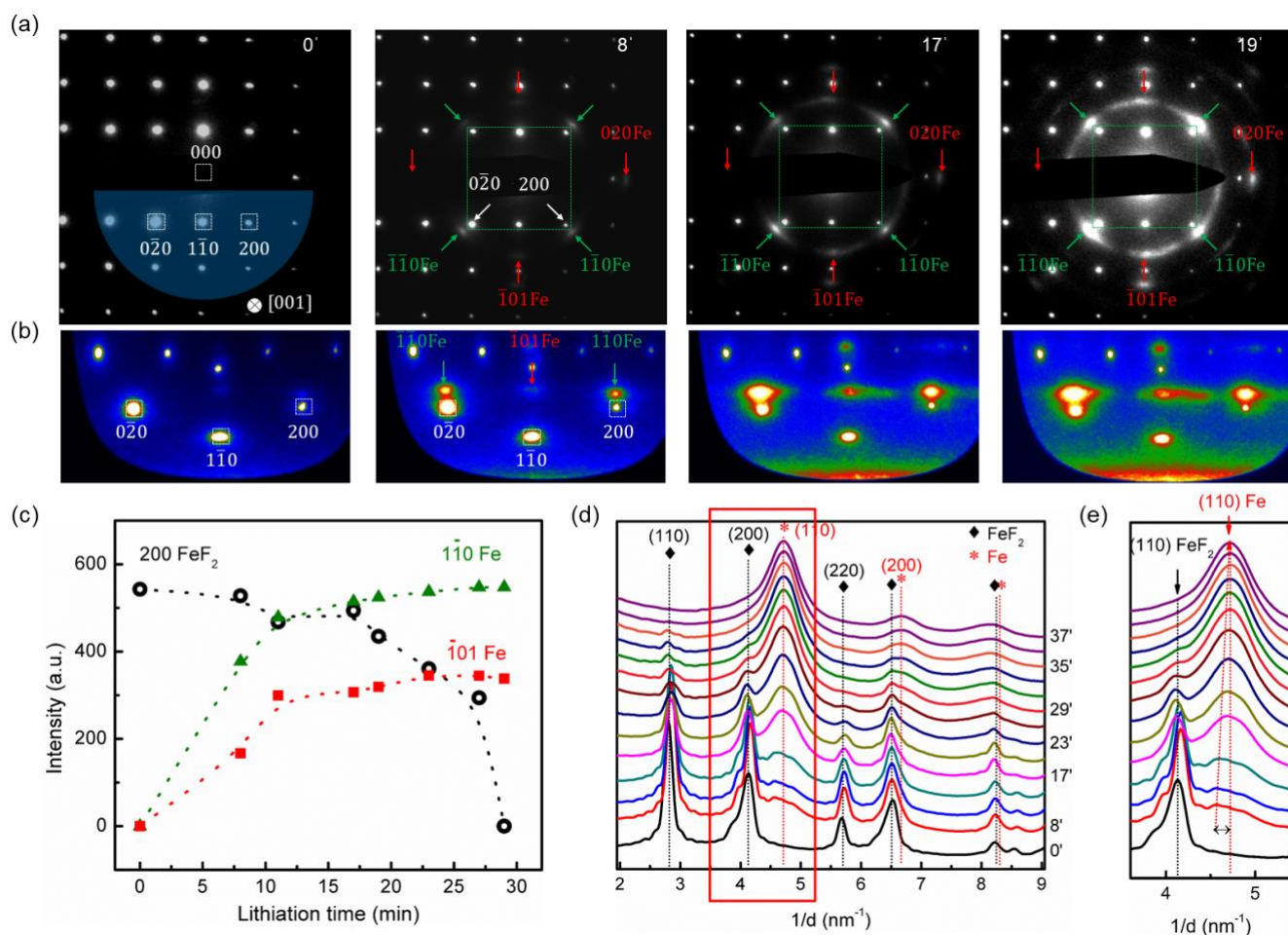


**Figure 2. Conversion-driven topotactic transformation in FeF<sub>2</sub> tracked by *in situ* electron diffraction** (See also Supporting Movie M2). (a) Representative electron diffraction patterns recorded from the white circled region in Figure 1(a), and (b) corresponding azimuthal projection images (See Supporting Movie M2 for the *time-resolved* diffraction patterns). The blue semi-circle area highlighted on the image in (a) shows the approximate radius and angles selected for the projection. (c) Comparison of intensity profiles between 110Fe (Case I) and 101Fe (Case-II) with respect to parent 200FeF<sub>2</sub>. (d) Radially integrated intensity profile as a function of lithiation time (between 0 to 37'). (e) Zoom-in view of the patterns from the red framed area in (d) showing the gradual growth of the (110)Fe peak during the lithiation process.

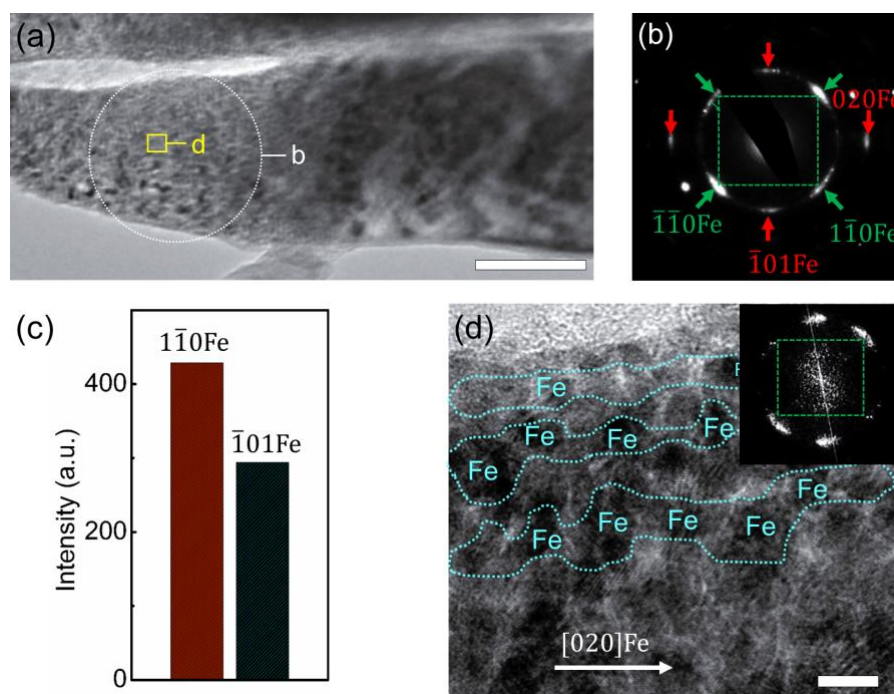


**Figure 3. Structural correlation between converted Fe and the parent  $\text{FeF}_2$ .** (a) Bright-field TEM image taken from an electrochemically lithiated  $\text{FeF}_2$  particle. Scale bar: 100 nm. (b) Electron diffraction pattern taken from the white circle area in (a). (c) Intensity histograms comparing  $1\bar{1}0\text{Fe}$  (Case I) and  $1\bar{0}1\text{Fe}$  (Case II) spots. (d) HRTEM image and corresponding FFT (inset) from the yellow framed area in (a). Scale bar: 5 nm.

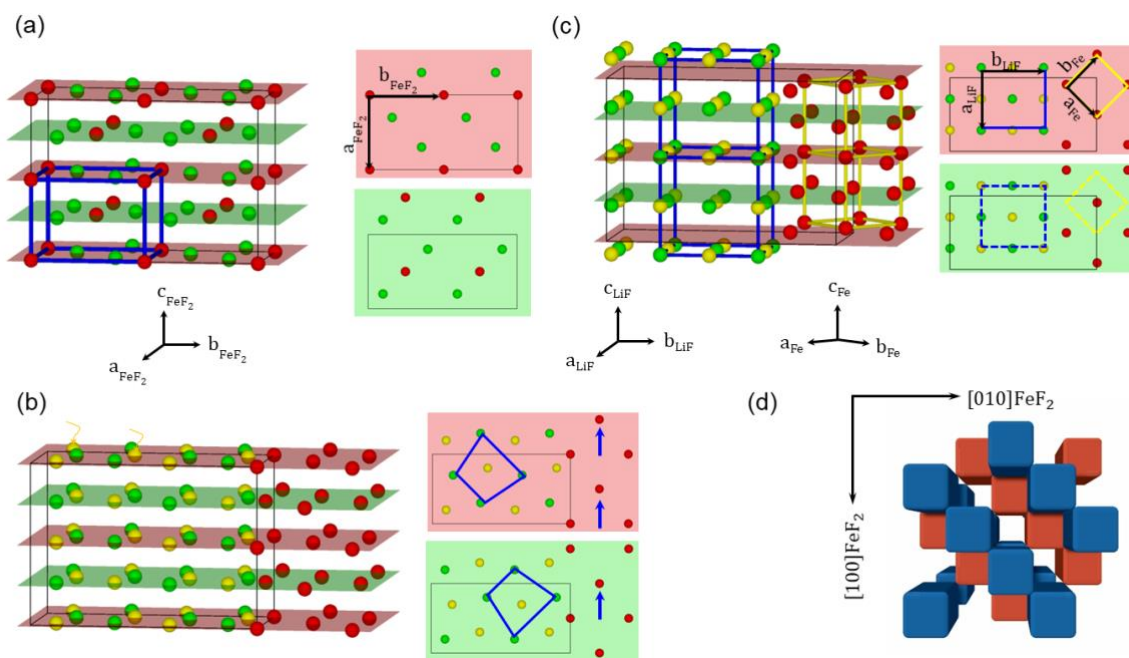


**Figure 4. Atomistic model of conversion-driven cationic displacement and topotactic transformation in FeF<sub>2</sub>.** (a) Schematic illustration of the structure of FeF<sub>2</sub> with Fe (red) and F (green). In the 3D view (left), the unit cell is outlined by thick blue lines. The thin black lines outline a 1×2×2 supercell. Alternative arrangement of Fe-F along [001] direction in the unit cell is shown in the red and green planes. (b) Li (yellow) insertion along [001] direction. (c) Expansion/contraction of Fe/LiF along different directions during conversion process. (d) Perspective view of the checkboard arrangement of the converted Fe domains, illustrated by the blue and red cubes at different height along [001] FeF<sub>2</sub> direction.